Research Article | Vol. 28, No. 21 / 12 October 2020 / Optics Express 31446

Optics EXPRESS

Reconfigurable reflective arrayed waveguide grating using optimization algorithms

JUAN FERNÁNDEZ,[1,*] JOAN FELIP,[1] BERNARDO GARGALLO,[1] JOSÉ DAVID DOMÉNECH,[1] DANIEL PASTOR,[2] CARLOS DOMÍNGUEZ-HORNA,[3] AND PASCUAL MUÑOZ[1,3]

[1] *VLC Photonics S.L., c/ Camino de Vera s/n - 46021 Valencia, Spain*
[2] *Photonic IC-group at the Photonics Research Labs, Universitat Politècnica de València, C/ Camino de Vera s/n, Valencia 46022, Spain*
[3] *Instituto de Microelectrónica de Barcelona (IMB-CNM, CSIC) C/ del Tilclers. Campus Universitat Autónoma de Barcelona (UAB), 08193 Cerdanyola del Vallés (Bellaterra), Spain*
[*] *juan.fernandez@vlcphotonics.com*
http://www.vlcphotonics.com/

Abstract: In this paper we report the experimental realization of a reconfigurable reflective arrayed waveguide grating on silicon nitride technology, using optimization algorithms borrowed from machine learning applications. A dozen of band-shape responses, as well as a spectral resolution change, are demonstrated in the optical telecom C-band, alongside a proof of operation of the same device in the O-band. In the context of programmable and reconfigurable integrated photonics, this building block supports multi-wavelength/band spectral shaping of optical signals that can serve to multiple applications.

© 2020 Optical Society of America under the terms of the OSA Open Access Publishing Agreement

1. Introduction

Integrated photonics is on the rise as a complementary technology to micro-electronics. Mainly driven in the last years by the need of more bits per second [1,2] from long haul telecom links, to short haul interconnects, photonic integration is now expanding to non-telecom application domains as civil engineering [3], bio and life sciences [4], environmental sensing [5–8] and automotive [9], among many other, as with more technology challenges ahead [10]. Integrated photonics is also expanding as microelectronics did, from application-specific to a programable or reconfigurable PICs [11], where different flavors arise, among them the Field Programmable Photonics Gate array (FPPGA) [12], artificial intelligence nano-photonics [13] , linear optical quantum computing [14], arbitrary optical waveform generation (AOWG) [15] among others. Reconfigurable band-pass shape optical filters are key for optical signal processing, for incumbent and emerging applications such as LIDAR, bio-sensing, microwave processing and telecommunications, to name a few.

Several integrated optics architectures have been explored, comprising micro-ring resonators in silicon [16,17] and silicon nitride [18], Mach-Zehnder Interferometers (MZIs) in silicon [19,20] and two arrayed waveguide gratings (AWGs) back-to-back in silica [21] and silicon [22]. Fontaine and co-workers reported a reconfigurable band-pass AWG in silica [23], with amplitude and phase tuning within the arms, demonstrating up to six different band-shapes. The number of previous works on tunable AWGs is humongous, but restricting the search to high-index contrast silicon photonics technology, most address phase tuning to correct phase errors and improve the passband shape and out-of-band floor [24,25]. In addition, other [26] report a minor re-shaping of the pass-band when tuning the center wavelength of the channels, through the phase of the AWG arms. Some works go beyond and make use of machine learning optimization algorithms [27,28] in their quest for perfecting the Gaussian response of AWGs. All the above works cited are for the optical telecom C-band. An interesting layout is the reflective AWG (RAW), where

#404267 https://doi.org/10.1364/OE.404267
Journal © 2020 Received 4 Aug 2020; revised 23 Sep 2020; accepted 24 Sep 2020; published 5 Oct 2020

Optics EXPRESS

a mirror is included halfway, and works using MEMS [29], distributed Bragg reflectors [30], photonic crystals [31], multimode interference reflectors [32] and metal [33] mirrors have been reported. Besides the footprint advantage, the mirror opens a new dimension for shaping the overall RAWG response, as we proposed earlier in [34].

In this paper we experimentally demonstrate for the first time to our knowledge, a reflective reconfigurable AWG (RRAWG) in silicon nitride technology, using tailored optimization algorithms borroed from machine learning applications. Twelve different band-pass shapes and spectral resolution change have been demonstrated in the C-band, and operation is also proved in the O-band. The paper is organized as follows. In section 2 we describe the device, the reconfiguration algorithm and provide its numerical validation. The experimental details, methods and validation of the RRAWG are given in section 3. The closing remarks and means for improvement are lastly introduced in section 4.

2. Reconfigurable reflective AWG with machine learning active reconfiguration

2.1. Device description

Our RRAWG incorporates an amplitude and phase tunable mirror in each arm, as sketched in Fig. 1(a). A static version with no tunable mirrors of the device was reported earlier in [34]. In this previous work by our group, no optimization of th response was provided, only the ability to do so with the RAWG Sagnac loop based layout was outlined, with some supporting simulation. Compared to [34], we have incorporated as mirrors a reflective version of a common Mach-Zehnder Interferometer (MZI), also known as Michelson interferometer, where each of the two arms is equipped with a thermo-optic phase shifter (TOPS) and terminated with a Sagnac Loop Reflector (SLR), as depicted in Fig. 1(b). The MZI is based on Multimode Interference (MMI) couplers (one for the arms, then two for the loop reflectors), so as to make the overall mirror as broadband as possible. The field amplitude and phase from these dual-drive MZIs can be controlled independently [35]. In regular AWGs, phase and amplitude errors are known to cause response degradation, and they may stem from design to fabrication imperfections. The tunable mirror is a reflective MZI as described, and despite all are done with the same layout, fabrication deviations (width, height and material properties of the cross-section) leave all these mirrors in an unknown starting point. Hence, without correction, the RRAWG passive response is naturally distorted. Traditionally phase trimming techniques have been applied to telecom (silica) AWGs, that set a static response to the device [36], but the active tuning capability of the tunable mirrors ideally can in first place alleviate up to some extent the fabrications deviations, and in second place provide the reconfiguration of the spectral response.

With respect to the actuators for the tunable mirrors, we resorted without loss of generality to the TOPS available in the employed photonic integration platform, but other actuation mechanisms may provide better features, in terms of footprint and speed. One of well-known inconveniences of TOPS is thermal management of the chip, which requires a temperature controller (TEC). Furthermore, when using arrays of TOPS (in some cases with several tens of them), in reconfigurable PICs, the thermal cross-talk adds to the complexity of converging to and stabilizing the optical response.

2.2. Reconfiguration strategy and implementation

For these complex reconfigurable PICs, different techniques and approaches are developed to reach the target response and stabilize the system along time. Several of them are described in the literature. Firstly, approaches based on obtaining the relative full-field amplitude and phase response of the temporal response of the complete system. One of the most used is the Optical Frequency Domain Reflectometry (OFDR), which can retrieve the full field response of virtually any passive integrated optics device along all the paths from input to output [37].

Optics EXPRESS

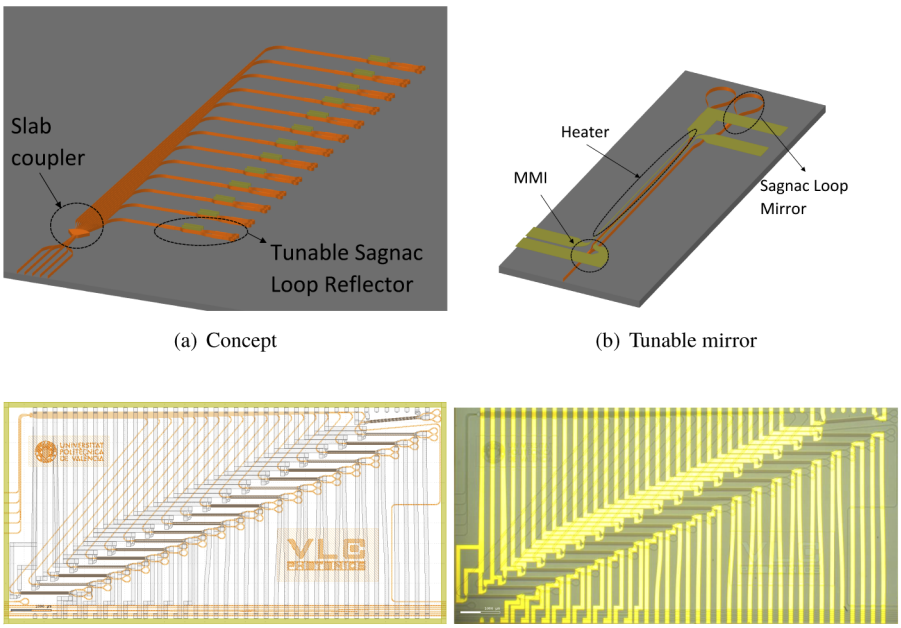

(a) Concept (b) Tunable mirror

(c) Layout (d) Fabricated chip

Fig. 1. Conceptual sketches for the RRAWG (a) and tunable mirrors (b). Device mask layout (c) and microscope photograph of the fabricated device (d) in a chip of 5x10 mm^2.

While it's probably the most powerful inspection technique, it requires heavy post-processing and ad-hoc configuration to retrieve the actual device response, which it's hard to make compatible to iterative real-time setting of the system response [27]. Secondly, some techniques to approach the ideal response of the array waveguide grating using Gerchberg-Saxton algorithms to recover the ideal phase in the array have been reported. These require combining the theoretical response with high level algorithms from hologram retrieval, provided the amplitude response very well known [38]. Additionally some works resort to algorithms to obtain the phase and the amplitude from the spectral response, but their performance is modest and they are oriented towards image recovery [39]. The third approach is ordinarily known as brute force [27], where the algorithms act simultaneously over all the free variables to obtain the complex response. There is an increasing use of these so-called machine learning techniques in multiple application domains, reconfigurable PICs among them, despite they may be suboptimal as compared to OFDR based approaches [27,40,41]. Addressing the full problem (full variable set, final target response) in a device, such as the one presented in this paper, wreaks havoc on the goal: convergence. The reason is they require iterative and continuous measurements, with an inherently non-linear problem, and a target response that evolves along time.

Generalist machine learning algorithms are extremely well-suited, albeit their potentially high computational cost, to solve very abstract problems with involved dependencies. Nonetheless, as is the case of our RRAWG, in most cases the internal structure of the problem is known, so the algorithms can be driven accordingly [42]. The (R)AWG response from one input to one output is formed by the wavelength-dependent constructive interference of the fields radiated from the arms. It is well-known that both sides of the slab coupler are transformed domains, in the most simplified approach represented by a spatial Fourier transform [43]. Another intrinsic property is the central arms receive more energy than the outer ones. Other practical aspect to consider when selecting an optimization algorithm, is optical misalignment along time of

Optics EXPRESS

the test setup. The algorithm has to allow pausing and resuming from a given point. Note that there are also other time-changing conditions in our device, due to the fact that thermal tuners influence each other (thermal cross-talk). Hence, some algorithms as neural networks need to restart because they rely on collecting statistical data to extract the behavior of the variables. In addition, algorithms not requiring the derivatives of the cost function are also preferred, since in our device, the changes in amplitude and phase of multiple interferers, may lead to local minima. Consequently, from all, we then selected the pattern search machine learning algorithm [44].

2.3. Numerical validation

A numerical model for the transfer function of the RRAWG was implemented using integral Fresnel for star coupler, and the length and effective indices of each section, as in our previous works [34,43]. The modeling of the tunable mirror accounts for the phase shifter measured electro-optic response. That includes a cubic relation between the electrical power dissipation and the electrical current due to self-heating (the ohmic resistance changes with the temperature / electrical current) [45]. The numerical model incorporates the ability to force random phase and amplitude errors [46] in the RRAWG arms, to synthesize responses similar to the ones obtained through fabrication.

Through simulation we explored first brute force optimization. We reproduced by simulation the response of an RRAWG with the same parameters than the fabricated device (see section 3.1). A cost function was defined, comparing the target and the intermediate response for a given wavelength range, and a set of currents in the TOPS. After some numerical experimentation, the cost function defined is similar to that used in microwave filter synthesis. It consists of the summation of the quadratic difference between the target response and the current response in logarithmic units [47]. This is a cost function that aims at sigmoid activation [48], and as it has been reported to have very good convergence for machine learning algorithms [49]. With this cost function and addressing the problem by brute force, i.e. all the TOPS currents at the same time, sub-optimal results, quite far from the target, were obtained. Next, and owing to the well-known internal structure described previously, we devised the following procedure. In a first step, the same brute force approach is followed, but the target is now to minimize the response over all wavelengths. This would be as switching-off all the RRAWG arms. Then, we progressively enable arms, starting with the first two in the center (owing to their natural larger energy). In this case the target spectral response imposed to the algorithm is far more simple than for N interferers, it is just the one for an MZI, and the algorithm only needs to deal with 4 TOPS. Upon convergence on this first step, the target function is replaced for that of a generalized MZI with three arms (the next with larger energy in the array), and consequently the number of free variables (TOPS currents) is then 6. But for four of them the initial values come from the previous successful minimization. The procedure is illustrated in Figs. 2(a)-(f). The first panel presents the target response for all the RRAWG channels in dashed lines, while the current response for the same is given in solid lines. The latter is calculated for a set of arbitrary starting phases in the arms. In panel (b), the result of minimizing the current response is shown. This provides a set of TOPS currents for all the arms. From this set, we show the target and current function after optimization for two arms (4 TOPS) as described, in panel (c), and following the optimization steps for 6 and 10 TOPS (3 and 5 arms enabled respectively) in (d) and (e). Finally, Fig. 2(f) provides the optimization result vs. target response when all the 38 TOPS (19 arms) are enabled.

Note that with our approach, the minimization step of Fig. 2(b) took 2768 iterations, and for all the other steps Figs. 2(c)-(f) another 11283 iterations. In general, all the simulations attempted with starting random amplitude and phase conditions, achieved minimization in approximately 3000 iterations, and optimization in about 12000 iterations (a comparison of the overall optimization approach, targets and performance, including the number of iterations in

Optics EXPRESS

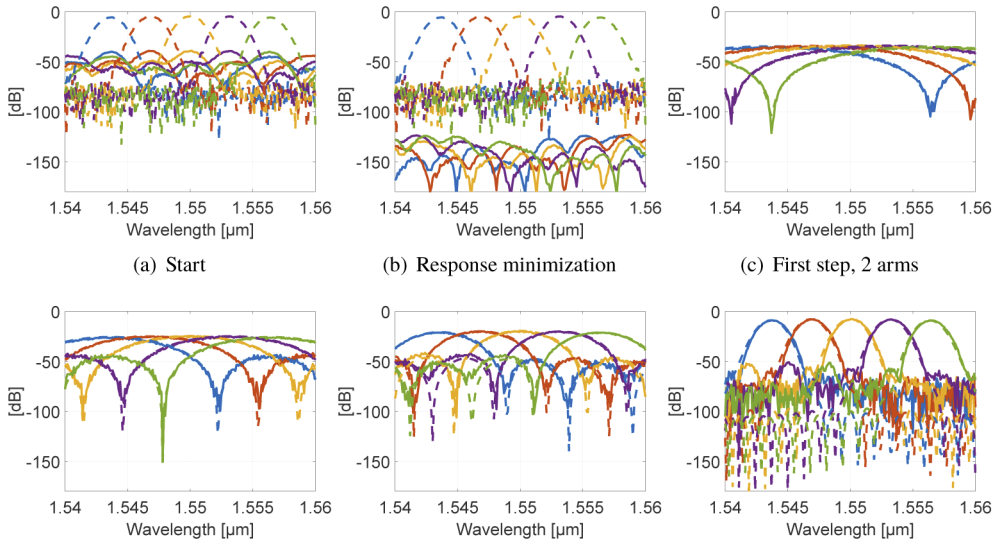

(a) Start (b) Response minimization (c) First step, 2 arms

(d) Second step, 3 arms (e) Third step, 5 arms (f) Final step, 19 arms

Fig. 2. Optimization algorithm step by step employing RRAWG response simulation. The panels show in solid and dashed lines the actual and target normalized responses (in logarithmic units) at a given step versus wavelength. Each of the color lines within the plots represents one of the five RRAWG channels. In (a) the starting situation is given, where the actual response is forced to differ heavily from the target, by including amplitude and phase errors. Panel (b) presents the first step in which the tuners are configured so as to 'switch-off' the device, i.e. minimizing the response, which is equivalent to bring all the arms out of constructive interference. From panels (c) to (e) the number of arms brought back to 'on-state' (constructive interference) is progressively increased. The last panel (f) shows the case for 19 arms enabled.

the experiment is given in Supplement 1). In this particular case each iteration took 11 seconds, from which the pattern search share was negligible, since all the time was mostly consumed by the RRAWG non-optimized simulation (i.e. the Fresnel numerical integral in a script language). However, in the experiments reported later on, one can adjust the analyzer span and resolution, to minimize spectra acquisition time, leading to optimization steps of 2-3 seconds in total. Despite one can reduce the optimization step time, just for reference, for tuners allowed to vary in a range of 75 mA, with a precision of 1 mA, the number of possible combinations would be of the order of 10^{118}, hence preventing the use of brute force. Upon confirmation the algorithms work on simulation, we proceeded to their use with the fabricated devices.

The algorithm flow, and the particular values and iterations required, are detailed further in Supplement 1. In short, it consists mainly of two steps: Step number 1, minimization, matching Fig. 2(b); and Step 2, restoring the response, iterated several times by progressively adding new variables (tuners) to the optimization algorithm, matching Fig. 2(c) to (f). See flowchart in Supplement 1.

3. Materials, methods and results

3.1. Device design and fabrication

The RRAWG was designed and fabricated using the CNM-VLC silicon nitride platform [50] whose technology is described in [51,52], through a Multi-Project Wafer run. Despite an SOI chip would have a footprint advantage, we selected nitride mainly the platform have the potential

Optics EXPRESS

to operate from visible to the mid-infrared [52], with properly scaled designs, thus covering a wider range of applications, that in turn may require re-programmable devices.The waveguide core has a cross-section of 1.0 μm x 0.3 μm patterned via reactive-ion etching on a film of silicon nitride deposited via low-pressure chemical vapor deposition, on top of a substrate of silica (2.5 μm height) obtained through wet oxidation of a silicon wafer. The waveguide core is cladded with plasma enhanced deposited silica (1.8 μm height). The TOPS have a width of 5 μm and are a bi-layer of Cr and Au patterned with lift-off, and 1.2 mm length. The RRAWG parameters for the manufactured devices are: center wavelength 1550 nm, 5 channels with spacing 3.2 nm and free spectral range (FSR) of 25.5 nm, slab coupler length 74.88 μm, arm length increment 49.24μm and the number of arms is 19, with bend radius 100 μm. The waveguides interfacing the slab coupler are up/down-tapered to 2 μm. They are placed following a traditional constant angle layout, 3 μm spacing over the grating circle, despite other placements can significantly improve the response [53]. The RRAWG footprint is 10x4.5 mm^2 (width x height) using and orthogonal layout as sketched in Fig. 1(a). The large footprint is due to the MZI based tunable mirrors, both by the large bending radius (conditions the arm spacing) and lengthy heaters (so as to make them reliable for a given width). At the outer part of each interferometer arm or heater, a shallow trench (just the cladding oxide removed) of 5 μm width is placed at distance of 13 μm. An additional trench is also present in the space between the two arms / heaters at 10 μm distance. With optimized TOPS cross-sections [54], or other tuning mechanisms, the footprint of the RRAWG could be significantly reduced. The chip is mounted on top of printed circuit board (PCB), and the TOPS pads are wire-bonded to the metal lines in the board, Fig. 3(a).

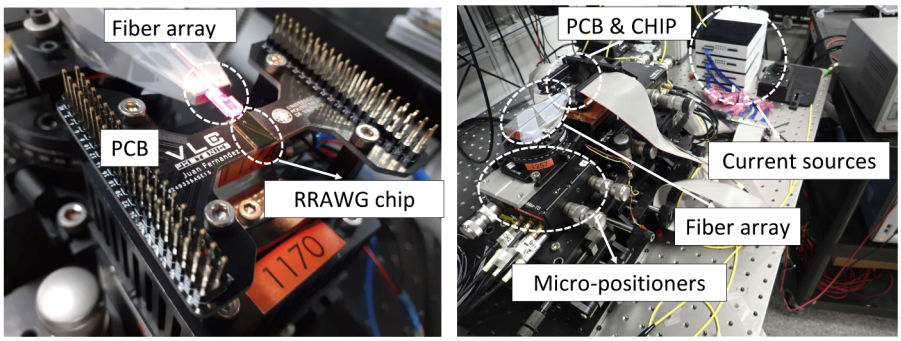

(a) Chip, PCB and fiber array (b) Setup general view

Fig. 3. Photographs of the mounted chip (a) and setup (b).

3.2. Laboratory setup

The characterization setup consists of two stages, one with the micro-positioners, a three axis motorized positioner and a manual positioner to control the yaw rotation angle, Fig. 3(b). The PCB with the chip sits on top of a thermally controlled chuck, held by the second stage. For the measurements, the fiber array is aligned manually in three steps.

First, the fiber array is yaw rotated until the fiber array edge is parallel to the chip. The other pitch and roll rotation angles do not need to be adjusted because the sample and the fiber array are carefully placed to be as parallel as possible. Second, a red light is used in two of the fibers in the array for visual alignment purposes. Third, once the fiber array is visually aligned with red light with the three-axis movement of the fiber array, a broadband infra-red light source (BBS) is connected to one of the fibers, whereas a power meter is connected at the other fiber of array. Hence, the position of the fiber array is optimized with the motorized stages to obtain the maximum power.

Optics EXPRESS

When the fiber array alignment is optimized, the power meter is replaced by an optical spectrum analyzer (OSA), which is used to record the spectra with a resolution of 20 pm for measurements in the optical C-band. To characterize in the O-band, the same procedure is used but the BBS is replaced by a Yenista tunable laser with a CT400 combiner, employed to synchronize the sweep and spectra recording. The spectra are recorded after each step where the TOPS are tuned to the currents provided by the pattern search algorithm. The TOPS currents are generated with a 4 multi-current LuzWavelabs modules, with 10 current sources each, Fig. 3(b).

3.3. Characterization results

In order to assess on the RAWG insertion loss, we captured the transmission spectra of straight waveguides. Despite coupling loss can thus be de-coupled, we still compared the straight waveguide transmission to that of the setup without chip. We obtained 3-3.5 dB/facet and 5-5.5 dB/facet insertion loss, for microscope objetives with 2.5x2.5 μm^2 mode-field diameter (MFD) and for ultra-high numerical aperture (UHNA7) fiber with 3.2x3.2 μm^2 MFD, respectively. The results are compatible with the MFD of the in/out waveguides 1.19x0.95 μm^2.

The peak insertion loss for the Gaussian optimized device was 15 dB below the transmission of the straight waveguide. From those, 5 dB correspond to 2.5 cm propagation and 2 dB to excess losses of the splitters used in the Michelson interferometer. Thus, the RAWG insertion loss is less than 8 dB considering part of it can be due to the fiber array not being optimally aligned.

The spectral response reconfiguration results are given in Fig. 4. The algorithm flow, and the particular values and iterations required, are detailed further in Supplement 1. Twelve different responses where synthesized. Except in (b), (k) and (l), only one FSR is shown for clearness, when comparing the synthesized responses to the target. Linear units are used in this case so as to clearly appreciate the differences. In the figure we show in the first place on panel (a) a regular Gaussian response, alongside the same response for the rest of the AWG channels in panel (b). From (c) to (g) the experimental results for the synthesis of flat, truncated cosine, Bessel, Lorentzian and decaying exponential responses are shown, all compared with their target function. Note that the starting point for all this is the previously optimized Gaussian response. All these experimental plots are collated in linear and logarithmic units in Fig. 5 (cf. with the theoretical proposal in Fig. 6 of our early work on Ref. [34]).

Other functions are synthesized in Figs. 4(h) to (j). In (h), the band-pass is unfolded to create a notch filter, whereas in (i) and (j) triangular shaped functions, isosceles and right triangle (ramp) are shown. A version of right triangle with opposite ramp was also demonstrated, but not shown for the sake of space. Panel (k) shows a Gaussian response synthesized with half FSR. Theoretically that would correspond to having two interleaved subarrays out of phase, as described in [55]. In conclusion, and from an application perspective, besides changing the shape of the bands, the RRAWG can reconfigure its spectral resolution. Furthermore, and owing to the broadband nature of silicon nitride on silica platform and the tunable mirrors used, responses where synthesized as well for the O-band, with two channels shown in panel (l). In this case, the other channels could not be properly measured, alignment was critical owing to a cross-section designed to work in the C-band, and light was guided through the substrate mainly, obfuscating the passing bands up to some extent.

As a general conclusion, by observing e.g. Fig. 5(b), the shape of the bands can be properly approximated, but indeed the overall response (band and out of band) is still not optimal. We believe there are several factors to investigate for further improvement, among them we would highlight two. Firstly, the ability of algorithm to find the best combination and how good that is. In this paper we used pattern search as a tool for a proof-of-concept, but we left unexplored how to assess on the machine learning algorithm performance itself. Secondly, design improvements to alleviate distortions (amplitude and phase) are not into place. These indeed would help the algorithm and overall strategy, recall we progressively set target responses from simple MZI to

Optics EXPRESS

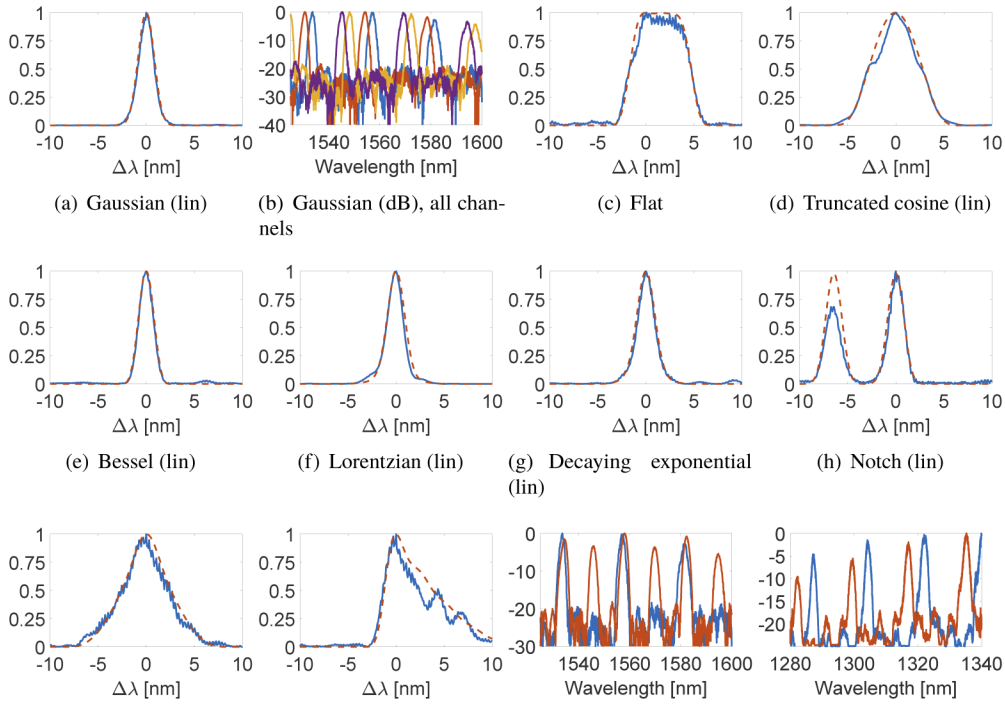

(a) Gaussian (lin) (b) Gaussian (dB), all channels (c) Flat (d) Truncated cosine (lin)

(e) Bessel (lin) (f) Lorentzian (lin) (g) Decaying exponential (lin) (h) Notch (lin)

(i) Triangular (lin) (j) Ramp right (lin) (k) x2 spectral resol. (dB) (l) Gaussian (dB), 1310 nm

Fig. 4. Spectral response reconfiguration results. All the responses are given normalized, either in linear (lin) or logarithmic (dB) units. For the linear representations, the horizontal axis is given as wavelength difference in nm from the peak center.

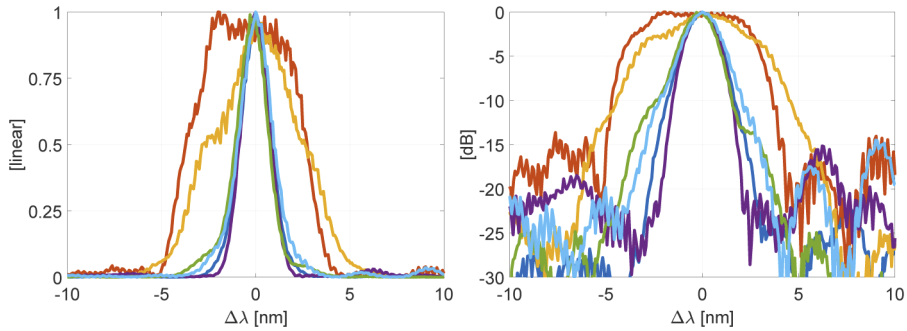

(a) Linear (b) Logarithmic

Fig. 5. Spectral response reconfiguration results compared. All the responses are given normalized, in linear (a) and logarithmic (dB) units versus the wavelength difference in nm from the peak center. The colors correspond to Gaussian (dark blue), flat (red), truncated cosine (orange), Bessel (purple), Lorentzian (green) and decaying exponential (light blue).

Optics EXPRESS

generalized MZI by enabling arms step by step. We believe the better the design, the better the match in the progressive steps and hence the final result. These design improvements should include waveguide widening in straight sections [56–58] and improved grating line waveguide placement in the slab coupler interface [53]. Last but not least, better thermal isolation (i.e. with deep trenches down to the silicon wafer) would certainly alleviate the optimization efforts.

4. Outlook and conclusions

In this work, we have presented the design, fabrication and experimental validation of an integrated reconfigurable reflective arrayed waveguide grating in silicon nitride technology. The reconfiguration was addressed by optimization algorithms borrowed from machine learning and adapted to the internal structure of our device. A dozen of different band-pass shapes have been demonstrated, alongside spectral resolution change in the C-band and operation in O-band. The device could be improved both in footprint, by using more compact bends and tuning elements, and performance, by refining the internal structure, waveguides and slab couplers, as well as by designing auxiliary elements, such as edge and MMI couplers, to operate broadband.

Funding

Ministerio de Economía y Competitividad (Industrial doctorate grant DI-15-08031, PID2019-110877GB-I00 BHYSINPICS, TEC2016-80385- P SINXPECT); H2020 Marie Skłodowska-Curie Actions (Training Network MICROCOMB (GA 812818)); Generalitat Valenciana (PROMETEO/2017/103).

Disclosures

The authors declare no conflicts of interest.

See Supplement 1 for supporting content.

References

1. F. Kish, V. Lal, P. Evans, S. W. Corzine, M. Ziari, T. Butrie, M. Reffle, H. Tsai, A. Dentai, J. Pleumeekers, M. Missey, M. Fisher, S. Murthy, R. Salvatore, P. Samra, S. Demars, N. Kim, A. James, A. Hosseini, P. Studenkov, M. Lauermann, R. Going, M. Lu, J. Zhang, J. Tang, J. Bostak, T. Vallaitis, M. Kuntz, D. Pavinski, A. Karanicolas, B. Behnia, D. Engel, O. Khayam, N. Modi, M. R. Chitgarha, P. Mertz, W. Ko, R. Maher, J. Osenbach, J. T. Rahn, H. Sun, K. Wu, M. Mitchell, and D. Welch, "System-on-chip photonic integrated circuits," IEEE J. Sel. Top. Quantum Electron. **24**(1), 1–20 (2018).
2. C. Doerr and L. Chen, "Silicon photonics in optical coherent systems," in *Proceedings of the IEEE*, (IEEE, 2018), pp. 1–11.
3. Y. E. Marin, T. Nannipieri, C. J. Oton, and F. D. Pasquale, "Current status and future trends of photonic-integrated FBG interrogators," J. Lightwave Technol. **36**(4), 946–953 (2018).
4. A. Fernández Gavela, D. Grajales García, J. Ramirez, and L. Lechuga, "Last advances in silicon-based optical biosensors," Sensors **16**(3), 285 (2016).
5. G. Roelkens, U. D. Dave, A. Gassenq, N. Hattasan, C. Hu, B. Kuyken, F. Leo, A. Malik, M. Muneeb, E. Ryckeboer, D. Sanchez, S. Uvin, R. Wang, Z. Hens, R. Baets, Y. Shimura, F. Gencarelli, B. Vincent, R. Loo, J. V. Campenhout, L. Cerutti, J. Rodriguez, E. Tournié, X. Chen, M. Nedeljkovic, G. Mashanovich, L. Shen, N. Healy, A. C. Peacock, X. Liu, R. Osgood, and W. M. J. Green, "Silicon-based photonic integration beyond the telecommunication wavelength range," IEEE J. Sel. Top. Quantum Electron. **20**(4), 394–404 (2014).
6. V. Singh, P. T. Lin, N. Patel, H. Lin, L. Li, Y. Zou, F. Deng, C. Ni, J. Hu, J. Giammarco, A. P. Soliani, B. Zdyrko, I. Luzinov, S. Novak, J. Novak, P. Wachtel, S. Danto, J. D. Musgraves, K. Richardson, L. C. Kimerling, and A. M. Agarwal, "Mid-infrared materials and devices on a si platform for optical sensing," Sci. Technol. Adv. Mater. **15**(1), 014603 (2014).
7. S. A. Holmstrom, T. H. Stievater, D. A. Kozak, M. W. Pruessner, N. Tyndall, W. S. Rabinovich, R. A. McGill, and J. B. Khurgin, "Trace gas Raman spectroscopy using functionalized waveguides," Optica **3**(8), 891–896 (2016).
8. L. Tombez, E. J. Zhang, J. S. Orcutt, S. Kamlapurkar, and W. M. J. Green, "Methane absorption spectroscopy on a silicon photonic chip," Optica **4**(11), 1322–1325 (2017).

Optics EXPRESS

9. M. J. Heck, "Highly integrated optical phased arrays: photonic integrated circuits for optical beam shaping and beam steering," Nanophotonics **6**(1), 93–107 (2017).
10. A. Karabchevsky, A. Katiyi, A. S. Ang, and A. Hazan, "On-chip nanophotonics and future challenges," Nanophotonics **9**(12), 3733–3753 (2020).
11. D. Pérez, I. Gasulla, L. Crudgington, D. J. Thomson, A. Z. Khokhar, K. Li, W. Cao, G. Z. Mashanovich, and J. Capmany, "Multipurpose silicon photonics signal processor core," Nat. Commun. **8**(1), 636 (2017).
12. D. P. López, A. L. Hernández, P. DasMahapatra, and J. Capmany, "Field-programmable photonic array for multipurpose microwave photonic applications," in *2019 International Topical Meeting on Microwave Photonics (MWP)*, (IEEE, 2019), pp. 1–4.
13. Q. Zhang, H. Yu, M. Barbiero, B. Wang, and M. Gu, "Artificial neural networks enabled by nanophotonics," Light: Sci. Appl. **8**(1), 42 (2019).
14. X. Qiang, X. Zhou, J. Wang, C. M. Wilkes, T. Loke, S. O'Gara, L. Kling, G. D. Marshall, R. Santagati, T. C. Ralph, J. Wang, J. L. O'Brien, M. G. Thompson, and J. C. Matthews, "Large-scale silicon quantum photonics implementing arbitrary two-qubit processing," Nat. Photonics **12**(9), 534–539 (2018).
15. M. Li, Y. Deng, J. Tang, S. Sun, J. Yao, J. Azaña, and N. Zhu, "Reconfigurable optical signal processing based on a distributed feedback semiconductor optical amplifier," Sci. Rep. **6**(1), 19985 (2016).
16. M. H. Khan, H. Shen, Y. Xuan, L. Zhao, S. Xiao, D. E. Leaird, A. M. Weiner, and M. Qi, "Ultrabroad-bandwidth arbitrary radiofrequency waveform generation with a silicon photonic chip-based spectral shaper," Nat. Photonics **4**(2), 117–122 (2010).
17. S. Liao, Y. Ding, J. Dong, S. Yan, X. Wang, and X. Zhang, "Photonic arbitrary waveform generator based on taylor synthesis method," Opt. Express **24**(21), 24390–24400 (2016).
18. L. Zhuang, "Flexible rf filter using a nonuniform scissor," Opt. Lett. **41**(6), 1118–1121 (2016).
19. S. Liao, Y. Ding, J. Dong, T. Yang, X. Chen, D. Gao, and X. Zhang, "Arbitrary waveform generator and differentiator employing an integrated optical pulse shaper," Opt. Express **23**(9), 12161–12173 (2015).
20. N. Zhou, S. Zheng, Y. Long, Z. Ruan, L. Shen, and J. Wang, "Reconfigurable and tunable compact comb filter and (de) interleaver on silicon platform," Opt. Express **26**(4), 4358–4369 (2018).
21. N. Fontaine, R. Scott, J. Cao, A. Karalar, W. Jiang, K. Okamoto, J. Heritage, B. Kolner, and S. Yoo, "32 phase× 32 amplitude optical arbitrary waveform generation," Opt. Lett. **32**(7), 865–867 (2007).
22. S. Zheng, Y. Long, D. Gao, Y. Luo, L. Wang, X. Cao, and J. Wang, "Chip-scale reconfigurable optical full-field manipulation: enabling a compact grooming photonic signal processor," ACS Photonics **7**(5), 1235–1245 (2020).
23. N. Fontaine, J. Yang, W. Jiang, D. Geisler, K. Okamoto, R. Huang, and S. Yoo, "Active arrayed-waveguide grating with amplitude and phase control for arbitrary filter generation and high-order dispersion compensation," in *2008 34th European Conference on Optical Communication*, (IEEE, 2008), pp. 1–2.
24. Y. Liu, Z. Li, D. Li, Y. Yao, J. Du, Z. He, and K. Xu, "Thermo-optic tunable silicon arrayed waveguide grating at 2-μm wavelength band," IEEE Photonics J. **12**, 1–8 (2020).
25. Y. Yang, X. Hu, J. Song, Q. Fang, M. Yu, X. Tu, and G.-Q. Lo Rusli, "Thermo-optically tunable silicon AWG with above 600 GHz channel tunability," IEEE Photonics Technol. Lett. **27**(22), 2351–2354 (2015).
26. S. Tondini, C. Castellan, M. Mancinelli, C. Kopp, and L. Pavesi, "Methods for low crosstalk and wavelength tunability in arrayed-waveguide grating for on-silicon optical network," J. Lightwave Technol. **35**(23), 5134–5141 (2017).
27. M. Gehl, D. Trotter, A. Starbuck, A. Pomerene, A. Lentine, and C. DeRose, "Active phase correction of high resolution silicon photonic arrayed waveguide gratings," Opt. Express **25**(6), 6320–6334 (2017).
28. P. Yuan, X.-G. Zhang, J.-M. An, P.-G. Yin, Y. Wang, and Y.-D. Wu, "Improved performance of a wavelength-tunable arrayed waveguide grating in silicon on insulator," Chin. Phys. Lett. **36**(5), 054204 (2019).
29. L. G. de Peralta, A. A. Bernussi, V. Gorbounov, J. Berg, and H. Temkin, "Control of center wavelength in reflective-arrayed waveguide-grating multiplexers," IEEE J. Quantum Electron. **40**(12), 1725–1731 (2004).
30. J. Zou, T. Lang, Z. Le, and J.-J. He, "Ultracompact silicon-on-insulator-based reflective arrayed waveguide gratings for spectroscopic applications," Appl. Opt. **55**(13), 3531–3536 (2016).
31. X. Zhang, J. Van Engelen, S. Reniers, Z. Cao, Y. Jiao, and A. Koonen, "Reflecting AWG by using photonic crystal reflector on indium-phosphide membrane on silicon platform," IEEE Photonics Technol. Lett. **31**(13), 1041–1044 (2019).
32. J. Wu and D. Gao, "Silicon reflective arrayed waveguide grating with multimode interference reflectors," in *2016 Asia Communications and Photonics Conference (ACP)*, (IEEE, 2016), pp. 1–3.
33. L. G. de Peralta, A. A. Bernussi, and H. Temkin, "Ultrafast response of arrayed waveguide gratings," IEEE J. Quantum Electron. **43**(6), 473–478 (2007).
34. B. Gargallo, P. Muñoz, R. Baños, A. L. Giesecke, J. Bolten, T. Wahlbrink, and H. Kleinjans, "Reflective arrayed waveguide gratings based on sagnac loop reflectors with custom spectral response," Opt. Express **22**(12), 14348–14362 (2014).
35. D. A. B. Miller, "Self-configuring universal linear optical component," Photonics Res. **1**(1), 1–15 (2013).
36. H. Yamada, K. Takada, Y. Inoue, Y. Ohmori, and S. Mitachi, "Statically-phase-compensated 10 GHz-spaced arrayed-waveguide grating," Electron. Lett. **32**(17), 1580–1582 (1996).
37. L. A. Bru, D. Pastor, and P. M. noz, "Integrated optical frequency domain reflectometry device for characterization of complex integrated devices," Opt. Express **26**(23), 30000–30008 (2018).

Optics EXPRESS

38. R. Gatdula and C. DeRose, "Negative feedback tuning of arrayed waveguide gratings," Tech. rep., Sandia National Lab.(SNL-NM), Albuquerque, NM (United States) (2015).
39. J. Fang and D. Savransky, "Amplitude and phase retrieval with simultaneous diversity estimation using expectation maximization," J. Opt. Soc. Am. A **35**(2), 293–300 (2018).
40. S. Tondini, C. Castellan, M. A. Medina, and L. Pavesi, "Automatic initialization methods for photonic components on a silicon-based optical switch," Appl. Sci. **9**(9), 1843 (2019).
41. D. Melati, Y. Grinberg, M. K. Dezfouli, S. Janz, P. Cheben, J. H. Schmid, A. Sánchez-Postigo, and D.-X. Xu, "Mapping the global design space of nanophotonic components using machine learning pattern recognition," Nat. Commun. **10**(1), 4775 (2019).
42. K. Yao, R. Unni, and Y. Zheng, "Intelligent nanophotonics: merging photonics and artificial intelligence at the nanoscale," Nanophotonics **8**(3), 339–366 (2019).
43. P. Muñoz, D. Pastor, and J. Capmany, "Modeling and design of arrayed waveguide gratings," J. Lightwave Technol. **20**(4), 661 (2002).
44. M. A. Abramson, "Pattern search algorithms for mixed variable general constrained optimization problems," Ph.D. thesis, Rice University (2002).
45. M. Bahadori, A. Gazman, N. Janosik, S. Rumley, Z. Zhu, R. Polster, Q. Cheng, and K. Bergman, "Thermal rectification of integrated microheaters for microring resonators in silicon photonics platform," J. Lightwave Technol. **36**(3), 773–788 (2018).
46. P. Muñoz, D. Pastor, J. Capmany, D. Ortega, A. Pujol, and J. R. Bonar, "AWG model validation through measurement of fabricated devices," J. Lightwave Technol. **22**(12), 2763 (2004).
47. P. Pramanick and P. Bhartia, *Modern RF and microwave filter design* (Artech House, 2016).
48. M. R. Zadeh, S. Amin, D. Khalili, and V. P. Singh, "Daily outflow prediction by multi layer perceptron with logistic sigmoid and tangent sigmoid activation functions," Water Resour. Manage. **24**(11), 2673–2688 (2010).
49. H. Zhang, T.-W. Weng, P.-Y. Chen, C.-J. Hsieh, and L. Daniel, "Efficient neural network robustness certification with general activation functions," in *Advances in neural information processing systems*, (Curran Associates, Inc., 2018), pp. 4939–4948.
50. VLC Photonics and Centro Nacional de Microelectrónica (CNM-VLC), "Silicon Nitride Photonic Integration Platform," http://www.imb-cnm.csic.es/index.php/en/clean-room/silicon-nitride-technology. Accessed: July-2020.
51. P. Muñoz, G. Micó, L. A. Bru, D. Pastor, D. Pérez, J. D. Doménech, J. Fernández, R. Baños, B. Gargallo, R. Alemany, A. M. Sánchez, J. M. Cirera, R. Mas, and C. Domínguez, "Silicon nitride photonic integration platforms for visible, near-infrared and mid-infrared applications," Sensors **17**(9), 2088 (2017).
52. P. Munoz, P. W. van Dijk, D. Geuzebroek, M. Geiselmann, C. Dominguez, A. Stassen, J. D. Doménech, M. Zervas, A. Leinse, C. G. Roeloffzen, B. Gargallo, R. Baños, J. Fernández, G. Micó Cabanaes, L. A. Bru, and D. Pastor, "Foundry developments toward silicon nitride photonics from visible to the mid-infrared," IEEE J. Sel. Top. Quantum Electron. **25**(5), 1–13 (2019).
53. J. Zou, Z. Le, J. Hu, and J.-J. He, "Performance improvement for silicon-based arrayed waveguide grating router," Opt. Express **25**(9), 9963–9973 (2017).
54. R. Alemany, P. Mu noz, D. Pastor, and C. Domínguez-Horna, "Thermo-optic phase tuners analysis and design for process modules on a silicon nitride," submitted to IEEE Journal of Selected Topics in Quantum Electronics (2020).
55. B. Gargallo and P. Muñoz, "Full field model for interleave-chirped arrayed waveguide gratings," Opt. Express **21**(6), 6928–6942 (2013).
56. J. Wang, Z. Sheng, L. Li, A. Pang, A. Wu, W. Li, X. Wang, S. Zou, M. Qi, and F. Gan, "Low-loss and low-crosstalk 8 × 8 silicon nanowire AWG routers fabricated with CMOS technology," Opt. Express **22**(8), 9395–9403 (2014).
57. J. Park, J. Joo, G. Kim, S.-W. Yoo, and S. Kim, "Low-crosstalk silicon nitride arrayed waveguide grating for the 800-nm band," IEEE Photonics Technol. Lett. **31**(14), 1183–1186 (2019).
58. U. Khan, M. Fiers, Y. Xing, and W. Bogaerts, "Experimental phase-error extraction and modelling in silicon photonic arrayed waveguide gratings," in *Silicon Photonics XV*, vol. 11285 G. T. Reed and A. P. Knights, eds., International Society for Optics and Photonics (SPIE, 2020), pp. 161–172.